1 Changes in black carbon emissions over Europe due to COVID-19

2 lockdowns

4 Nikolaos Evangeliou[1,*], Stephen M. Platt[1], Sabine Eckhardt[1], Cathrine Lund Myhre[1], Paolo

5 Laj[2,3,4], Lucas Alados-Arboledas[5,6], John Backman[7], Benjamin T. Brem[8], Markus Fiebig[1],

6 Harald Flentje[9], Angela Marinoni[10], Marco Pandolfi[11], Jesus Yus-Dìez[11], Natalia Prats[12], Jean

7 P. Putaud[13], Karine Sellegri[14], Mar Sorribas[15], Konstantinos Eleftheriadis[16], Stergios Vratolis[16],

8 Alfred Wiedensohler[17], Andreas Stohl[18]

10 [1]Norwegian Institute for Air Research (NILU), Department of Atmospheric and Climate

11 Research (ATMOS), Kjeller, Norway.

12 [2]University of Grenoble Alpes, CNRS, IRD, Grenoble-INP, IGE, 38000 Grenoble, France.

13 [3]CNR-ISAC, National Research Council of Italy – Institute of Atmospheric Sciences and

14 Climate, Bologna, Italy.

15 [4]University of Helsinki, Atmospheric Science division, Helsinki, Finland.

16 [5]Andalusian Institute for Earth System Research (IISTA-CEAMA), Granada, Spain.

17 [6]Department of Applied Physics, University of Granada, Granada, Spain.

18 [7]Atmospheric Composition Research, Finnish Meteorological Institute, Helsinki, Finland.

19 [8]Laboratory of Atmospheric Chemistry, Paul Scherrer Institute, Villigen PSI, Switzerland.

20 [9]Deutscher Wetterdienst, Meteorologisches Observatorium Hohenpeissenberg, Albin-

21 Schwaiger-Weg 10, 82383 Hohenpeissenberg, Germany.

22 [10]Institute of Atmospheric Sciences and Climate, National Research Council of Italy (ISAC-

23 CNR), 40121, Bologna, Italy.

24 [11]Institute of Environmental Assessment and Water Research IDAEA-CSIC, C/Jordi Girona

25 18-26, Barcelona 08034, Spain.

26 [12]Izaña Atmospheric Research Center, State Meteorological Agency (AEMET), C/La Marina

27 20, 38001, Tenerife, Spain.

28 [13]European Commission, Joint Research Centre (JRC), Via Enrico Fermi 2749, Ispra (VA)

29 21027, Italy.

30 [14]Laboratoire de Météorologie Physique, UMR6016, CNRS/UBP, 63178 Aubière, France.

31 [15]El Arenosillo Atmospheric Sounding Station, Atmospheric Research and Instrumentation

32 Branch, National Institute for Aerospace Technology, 21130 Huelva, Spain.

33   [16]Environmental Radioactivity Lab, Institute of Nuclear & Radiological Sciences &

34   Technology, Energy & Safety, NCSR "Demokritos", Ag. Paraskevi, Athens, Greece.

35   [17]Department Experimental Aerosol and Cloud Microphysics, Leibniz Institute for

36   Tropospheric Research, Leipzig, Germany.

37   [18]Department of Meteorology and Geophysics, University of Vienna, UZA II,

38   Althanstraße 14, 1090 Vienna, Austria.

39

40   * Corresponding author: N. Evangeliou (Nikolaos.Evangeliou@nilu.no)

41

42

Abstract

43

44 Following the emergence of the severe acute respiratory syndrome coronavirus 2 (SARS-
45 CoV-2) responsible for COVID-19 in December 2019 in Wuhan (China) and its spread to the
46 rest of the world, the World Health Organization declared a global pandemic in March 2020.
47 Without effective treatment in the initial pandemic phase, social distancing and mandatory
48 quarantines were introduced as the only available preventative measure. Despite the
49 socioeconomic impacts, air quality improved due to lower pollutant emissions. Here we
50 investigate the effects of the COVID-19 lockdowns on ambient black carbon (BC), which
51 affects climate and damages health, using in-situ observations from 17 European stations in a
52 Bayesian inversion framework. BC emissions declined by 11% in Europe (20% in Italy, 32%
53 in Germany, 20% in Spain) during lockdown compared to the same period in the previous five
54 years. BC temporal variation in the countries enduring the most drastic restrictions showed the
55 most distinct lockdown impacts. Increased particle light absorption in at the beginning of the
56 lockdown, confirmed by assimilated satellite and remote sensing data, suggests residential
57 combustion was the dominant BC source. Accordingly, in Central and Eastern Europe, which
58 experienced lower than average temperatures, BC was elevated compared to the previous five
59 years. Except for the comparison of BC emissions in the lockdown with the previous five years,
60 an immediate decrease was also seen, as compared with the period before the lockdown, which
61 averaged about 10% over Europe. Such a decrease was not seen in the previous years, which
62 also confirms an impact on BC emissions from COVID-19.

63

64

1 Introduction

The identification of the severe acute respiratory syndrome coronavirus 2 (SARS-CoV-2 or COVID-19) in December 2019 (WHO, 2020) in Wuhan (China) and its subsequent transmission to South Korea, Japan, and Europe (initially mainly Italy, France and Spain) and the rest of the world led the World Health Organization to declare a global pandemic by March 2020 (Sohrabi et al., 2020). Although the symptoms are normally mild or not even detected for most of the population, people with underlying diseases or elderly are very vulnerable showing complications that can lead to death (Huang et al., 2020). Considering the lack of available treatment and vaccination to combat further spread of the virus, the only prevention measures included strict social, travel and working restrictions in a so-called lockdown period that lasted for several weeks (mid-March to end of April 2020 for most of Europe). The most drastic measures were taken in China, where the outbreak started, in Italy that faced large human losses and later in the United States. Despite all these restriction, still six months after the first lockdown, several countries are reporting severe human losses due to the virus (John Hopkins University of Medicine, 2020).

Despite the dramatic health and socioeconomic consequences of COVID-19 lockdowns, their environmental impact might be beneficial. Bans on mass gatherings, mandatory school closures, and home confinement (He et al., 2020; Le Quéré et al., 2020) during lockdowns have all resulted in lower traffic-related pollutant emissions and improved air quality in Asia, Europe and America (Adams, 2020; Bauwens et al., 2020; Berman and Ebisu, 2020; Conticini et al., 2020; Dantas et al., 2020; Dutheil et al., 2020; He et al., 2020; Kerimray et al., 2020; Le et al., 2020; Lian et al., 2020; Otmani et al., 2020; Sicard et al., 2020; Zheng et al., 2020). The restrictions also present an opportunity to evaluate the cascading responses from the interaction of humans, ecosystems, and climate with the global economy (Diffenbaugh et al., 2020).

Strongly light absorbing black carbon (BC, or 'soot'), is produced from incomplete combustion of carbonaceous fuels e.g. fossil fuels, wood burning, biofuels (Bond et al., 2013). By absorbing solar radiation, it warms the air, reduces tropical cloudiness (Ackerman, 2000) and atmospheric visibility (Jinhuan and Liquan, 2000). BC causes pulmonary diseases (Wang et al., 2014a), may act as cloud condensation nuclei affecting cloud formation and precipitation (Wang et al., 2016) and contributes to global warming (Bond et al., 2013; Myhre et al., 2013; Wang et al., 2014a). When deposited on snow, it reduces snow albedo (Clarke and Noone, 1985; Hegg et al., 2009) accelerating melting. Since BC is both climate relevant and strongly

97 linked to anthropogenic activity, it is important to determine the effects of the COVID-19

98 lockdowns thereon.

99 Here, we present a rigorous assessment of temporal and spatial changes BC emissions

100 over Europe (including Middle East and parts of North Africa), combining in situ observations

101 from the Aerosol, Clouds and Trace Gases Research Infrastructure (ACTRIS) network and

102 state-of-the-art emission inventories within a Bayesian inversion. We validate our results with

103 independent satellite data and compare them to inventories and baseline and optimized

104 emissions calculated for previous years.

105 2 Methods

106 2.1 Particle light absorption measurements

107 The measurement sites contributing data to this paper are regional background sites

108 (except for one site in Germany) and all contribute to the research infrastructure Aerosol,

109 Clouds and Trace Gases Research Infrastructure (ACTRIS), and the networks European

110 Monitoring and Evaluation Program (EMEP) and Global Atmosphere Watch (GAW). The

111 measurement data used for the period 2015 - May 2020 consist of hourly-averaged, quality-

112 checked, particle light absorption measurements. The quality assurance and quality control

113 correspond to the Level 2 requirements for ACTRIS, EMEP and GAW data, as described in

114 detail in Laj et al. (2020).

115 All absorption measurements within ACTRIS and EMEP are taken using a variety of

116 filter-based photometers: Multi-Angle Absorption Photometers (MAAP), Particle Soot

117 Absorption Photometers (PSAP) Continuous Light Absorption Photometers (CLAP), and the

118 Aethalometer (AE31). Information on instrument type at the various sites are included in Table

119 1 and procedures for harmonization of measurement protocols to produce comparable data seta

120 are described in Laj et al. (2020) in detail. Zanatta et al. (2016) suggested that a MAC value of

121 10 m^2 g^{-1} (geometric standard deviation of 1.33) at a wavelength of 637 nm can be considered

122 to be representative of the mixed boundary layer at European ACTRIS background sites, where

123 BC is expected to be internally mixed to a large extent. Assuming an absorption Ångström

124 exponent (AAE) is equal to unity, i.e. assuming no change in MAC for different sources (Zotter

125 et al., 2017), we extrapolated the MACs at 637 nm ($MAC_{@\lambda 1}$) to the measurement wavelengths

126 of our study ($MAC_{@\lambda 2}$) using the following equation:

127
$$MAC_{@\lambda 2} = MAC_{@\lambda 1}\left(\frac{\lambda 1}{\lambda 2}\right)^{AAE} \xrightarrow{yields} MAC_{@\lambda 2} = 10\left(\frac{637}{\lambda 2}\right)^{1} \qquad (1)$$

128 following Lack and Langridge (2013). The resulting MAC values for each measurement

129 station are shown in Table 1.

2.2 Source – receptor matrix (SRM) calculations

131   Source – receptor matrices (SRMs), also known as "footprint emission sensitivities" or

132 "footprints" for each of the 17 receptor sites (Table 1) were calculated using the Lagrangian

133 particle dispersion model FLEXPART version 10.4 (Pisso et al., 2019). The model releases

134 computational particles that are tracked backward in time based on 3-hourly operational

135 meteorological analyses from the European Centre for Medium-Range Weather Forecasts

136 (ECMWF) with 137 vertical layers and a horizontal resolution of 1°×1°. The tracking of BC

137 particles includes gravitational settling for spherical particles with an aerosol mean diameter of

138 0.25 μm and a logarithmic standard deviation of 0.3 and a particle density of 1500 kg m^{-3} (Long

139 et al., 2013). FLEXPART also simulates dry and wet deposition (Grythe et al., 2017),

140 turbulence (Cassiani et al., 2014), unresolved mesoscale motions (Stohl et al., 2005) and

141 includes a deep convection scheme (Forster et al., 2007). SRMs were calculated for 30 days

142 backward in time, at temporal intervals that matched measurements at each receptor site. This

143 backward tracking is sufficiently long to include almost all BC sources that contribute to surface

144 concentrations at the receptors given a typical atmospheric lifetime of 3–11 days (Bond et al.,

145 2013).

2.3 Bayesian inverse modelling

147   The Bayesian inversion framework FLEXINVERT+ described in detail in Thompson

148 and Stohl (2014) was used to optimize emissions of BC before (January to mid-March) and

149 during the COVID-19 lockdown period in Europe (mid-March to end of April). The algorithm

150 finds the optimal emissions, which lead to FLEXPART-modelled concentrations that better

151 match the observations considering the uncertainties for observations, prior emissions and

152 SRMs. The optimized (a posteriori) emissions are those that minimize the cost function:

153
$$J(x) = \frac{1}{2}(x - x_b)^T \mathbf{B}^{-1}(x - x_b) + \frac{1}{2}(y - \mathbf{H}x)^T \mathbf{R}^{-1}(y - \mathbf{H}x) \qquad (2)$$

154 where $\mathbf{H}$ is the Jacobian matrix of SRMs, y the vector of observed BC concentrations, x and

155 x_b the vectors of optimized and prior emissions, respectively, while $\mathbf{B}$ and $\mathbf{R}$ are the error

156 covariance matrices for the prior emissions and the observations, respectively. The most

157 probable posterior emissions, x are given by the following equation (Tarantola, 2005):

158
$$x = x_b + \mathbf{B}\mathbf{H}^T(\mathbf{H}\mathbf{B}\mathbf{H}^T + \mathbf{R})^{-1}(y - \mathbf{H}x_b) \qquad (3)$$

159   Here, posterior emissions were calculated weekly between 1 January and 30 April 2020.

160   To show potential differences on the signal from the 2020 restrictions, we calculated the

161   posterior emissions of BC for the same periods in the years 2015–2019. The aggregated

162   inversion grid (25°N–75°N and 10°W–50°E) and the average SRM for inversions are shown in

163   Figure 1, while the measurement stations are listed in Table 1. The variable grid uses high

164   resolution at regions, where there are many stations and hence strong contribution from

165   emissions, while it lowers resolution at regions that lack measurement stations following a

166   method proposed by Stohl et al. (2010)

167   Theoretically, the algorithm can calculate negative posterior emissions, which are

168   physically unlikely. To tackle this problem, an inequality constraint was applied on the

169   emissions following the method of Thacker (2007) that applies the constraint as "error-free"

170   observations:

171
$$\hat{x} = x + \mathbf{AP^T(PAP^T)^{-1}}(c - \mathbf{P}x) \qquad (4)$$

172   where $\mathbf{A}$ is the posterior error covariance matrix, $\mathbf{P}$ is a matrix operator to select the variables

173   that violate the inequality constraint, and c is a vector of the inequality constraint, which in this

174   case is zero.

175   We evaluated the assumptions made on the error covariance matrices for the prior

176   emissions and the observations using the reduced χ^2 statistics ($\mathbf{B}$ and $\mathbf{R}$). When χ^2 is equal to

177   unity, the posterior solution is within the limits of the prescribed uncertainties. The latter is the

178   value of the cost function at the optimum and is equivalent to the weighted sum of squares

179   divided by the number of observations (Thompson et al., 2015). In the inversions performed

180   here, the calculated χ^2 values were between 0.8 and 1.5 indicating that the chosen uncertainty

181   parameters are close to the ideal ones. The number of measurements used in each inversion was

182   equal to 12538 from 17 stations. To select the inversion that provides the most statistically

183   significant result, an evaluation of the improvement in the posterior modelled concentrations,

184   with respect to the prior ones, against the observations was performed (Figure 2). The resulting

185   values of each of the statistical measures that were performed are given in detail in Table 2.

186   Note that this is not a validation of the posterior emissions, because the comparison is only done

187   for the observations that were included in the inversion (dependent observations), and the

188   inversion algorithm has been designed to reduce the model–observation mismatches. This

189   means that the reduction of the posterior concentration mismatches to the observations is

190   determined by the weighting that is given to the observations with respect to the prior emissions.

191   A proper validation of the posterior emissions is performed against observations that were not

192   included in the inversion (independent observations) in Results section.

2.4 Prior emissions

193

194 As a priori emissions in the inversions, the ECLIPSE version 5 and 6 (Evaluating the
195 CLimate and Air Quality ImPacts of ShortlivEd Pollutants) (Klimont et al., 2017), EDGAR
196 (Emissions Database for Global Atmospheric Research) version HTAP_v2.2 (Janssens-
197 Maenhout et al., 2015), ACCMIP (Emissions for Atmospheric Chemistry and Climate Model
198 Intercomparison Project) version 5[ref] (Lamarque et al., 2013) and PKU (Peking University)
199 (Wang et al., 2014b) were used (Figure 3). All inventories include the basic emission sectors
200 (e.g., waste burning, industrial combustion and processing, all means of transportation (aerial,
201 surface, ocean), energy conversion, residential and commercial combustion (see references
202 therein). Biomass burning emissions were adopted from the Global Fire Emissions Database,
203 Version 4.1s (GFEDv4.1s)(Giglio et al., 2013).

2.5 MERRA-2 (Modern-Era Retrospective Analysis for Research and Applications

204

205 Version 2)

206 The MERRA-2 reanalysis dataset for BC (Randles et al., 2017) assimilates bias-corrected
207 AOD from Moderate Resolution Imaging Spectroradiometer (MODIS), Advanced Very High
208 Resolution Radiometer (AVHRR) instruments, Multiangle Imaging SpectroRadiometer
209 (MISR) and Aerosol Robotic Network (AERONET) with the Goddard Earth Observing System
210 Model Version 5 (GEOS-5). BC and other aerosols in MERRA-2 are simulated with the
211 Goddard Chemistry, Aerosol, Radiation and Transport (GOCART) model and delivered in
212 hourly to monthly temporal resolution and 0.5°×0.625° spatial. The product has been validated
213 for AOD, PM and BC extensively (Buchard et al., 2017; Qin et al., 2019; Randles et al., 2017;
214 Sun et al., 2019). Ångström exponent (AE), a measure of how the AOD changes relative to the
215 various wavelength of light, is derived here from AOD469, AOD550, AOD670, and AOD865,
216 by fitting the data to the linear transform of Ångström's empirical expression:

217
$$\tau_\lambda = \tau_{\lambda_0}(\frac{\lambda}{\lambda_0})^{-a} \qquad (5)$$

218 where τ_λ is the known AOD at wavelength λ (in nm), τ_{λ_0} is the AOD at 1000 nm, and α stands
219 for AE (Gueymard and Yang, 2020).

2.6 Absorption Ångström exponent from AErosol RObotic NETwork (AERONET)

220

221 data

222 Aerosol composition over Europe during the COVID-19 lockdown was confirmed using
223 the AERONET data (Holben et al., 1998). AERONET provides globally distributed

224 observations of spectral aerosol optical depth (AOD), inversion products, and precipitable

225 water in diverse aerosol regimes. The AE for a spectral dependence of 440-870 nm is related to

226 the aerosol particle size. Values less than 1 suggest an optical dominance of coarse particles

227 corresponding to dust, ash and sea spray aerosols, while values greater than one imply

228 dominance of fine particles such as smoke and industrial pollution (Eck et al., 1999). We chose

229 data from five stations covering Western, Central and Eastern Europe, for which cloud-free

230 measurements exist for the lockdown period, namely Ben Salem (9.91°E, 35.55°N), Minsk

231 (27.60°E, 53.92°N), Montsec (0.73°E, 42.05°N), MetObs Lindenberg (14.12°E, 52.21°N) and

232 Munich University (11.57°E, 48.15°N). We used Level 1.5 absorption AE (AAE)

233 measurements for the COVID-19 lockdown period (14 March to 30 April 2020).

234 **2.7 Statistical measures**

235 For the performance evaluation of the inversion results against dependent (observations

236 that were included in the inversion) and independent observations (observations that were not

237 included in the inversion), four different statistical quantities were used:

238 (1) Pearson's correlation coefficient:

239
$$R_{mo} = \frac{n\sum_{i=1}^{n} m_i o_i - \sum_{i=1}^{n} m_i \sum_{i=1}^{n} o_i}{\sqrt{n\sum_{i=1}^{n} m_i^2 - (\sum_{i=1}^{n} m_i)^2}\sqrt{n\sum_{i=1}^{n} o_i^2 - (\sum_{i=1}^{n} o_i)^2}} \qquad (6)$$

240 where n is sample size, m and o the individual sample points for model concentrations and

241 observations indexed with i.

242 (2) The normalized root mean square error (nRMSE):

243
$$nRMSE = \frac{\sqrt{\sum_{i=1}^{n} \frac{1}{n}(m_i - o_i)^2}}{o_i^{max} - o_i^{min}} \qquad (7)$$

244 (3) The mean fractional bias MFB was selected as a symmetric performance indicator that gives

245 equal weights to under- or over-estimated concentrations (minimum to maximum values range

246 from -200% to 200%) and is defined as:

247
$$MFB = \frac{1}{n}\frac{\sum_{i=1}^{n}(m_i - o_i)}{\sum_{i=1}^{n}(\frac{m_i + o_i}{2})} \qquad (8)$$

248 (4) The mean absolute error was computed normalized ($nMAE$) over the average of all the

249 actual values (observations here), which is a widely used simple measure of error:

250
$$nMAE = \frac{\sum_{i=1}^{n}|m_i - o_i|}{\sum_{i=1}^{n} o_i} \qquad (9)$$

2.8   Region definitions

All country and regional masks are publicly available. Regions used for statistical processing purposes were adopted from the United Nations Statistics Division (https://unstats.un.org/home/). Accordingly, Northern Europe includes UK, Norway, Denmark, Sweden, Finland, Iceland, Estonia, Latvia and Lithuania. Southern Europe includes Spain, Italy, Greece, Slovenia, Croatia, Bosnia, Serbia, Albania and North Macedonia. Western Europe is defined by France, Belgium, Holland, Germany, Austria and Switzerland. Eastern Europe includes Poland, Czechia, Slovakia, Hungary, Romania, Bulgaria, Moldova, Ukraine, Belarus and Russia.

3   Results

3.1   Optimized (posterior) emissions from Bayesian inversion

We performed five inversions for BC over Europe for 1st January- 30th April 2020, each with different prior emissions from ECLIPSE version 5 and 6, EDGAR version HTAP_v2.2, ACCMIP version 5 and PKU (Figure 3). Total prior emissions of BC in Europe from the five emission inventories for the period of the inversion ranged between 192-377 kt. We evaluated the assumptions made on the error covariance matrices for the prior emissions and the observations using the reduced χ^2 statistic (**B** and **R**, see section 2.3). When χ^2 is equal to unity, the posterior solution is within the limits of the prescribed uncertainties. The performance of the inversions with the five different prior inventories was evaluated using four statistical parameters (see section 2.7). The best performance of the inversions was achieved using ECLIPSEv6 (Table 2 and Figure 2) with the smallest $nRMSE$ (0.073) value, the largest Pearson's R^2 (0.60), the closest to zero MFB value (0.03) and the smallest $nMAE$ (714). Therefore, all the results presented below correspond to this inversion.

Emissions were calculated to be 191 kt in the inversion domain or approximately 20% smaller than those in ECLIPSEv6 (239 kt) (Figure 4). Note that the aforementioned numbers refer to the whole inversion domain (not only Europe) and the whole study period (January – April 2020). The largest posterior decreases were found in Eastern Europe, where emissions dropped from 35 to 29 kt. Western European emissions of BC declined by almost 11% (from 45 to 40 kt), as those in Scandinavian countries (from 8.7 to 6.4 kt). Finally, in Southern Europe (Spain, Italy, Greece) the posterior emissions also decreased by 21% relative to the priors (from 61 to 48 kt). The largest country decreases were seen in France (from 14 to 8.2 kt), Italy (from

282 8.0 to 5.9 kt), UK (from 4.4 to 3.1 kt) and Germany (from 4.5 to 4.1 kt). Surprisingly, BC

283 emissions were slightly enhanced in Poland (from 21 to 23 kt), and Spain (from 6.3 to 7.5 kt)

284 were slightly enhanced. Note that although posterior emissions may only imply error in the

285 prior emissions, we demonstrate that the decrease was in fact due to the COVID-19 lockdowns

286 in the next section (3.2).

3.2 Comparison with previous years

288 We also performed inversions for 2015–2019 for the same period as the 2020 lockdowns

289 (January- April) using almost the same measurement stations and keeping the same settings.

290 The difference in BC emissions during the lockdown in 2020 (14 March to 30 April) from the

291 respective emissions during the same period in 2015–2019 (14 March to 30 April) are shown

292 in Figure 5 (a, emission anomaly) together with the gross domestic product (GDP) (Kummu et

293 al., 2020) (b) , and (c) temperature anomaly from ERA-5 (Copernicus Climate Change Service

294 (C3S), 2020) for the same period as the emission anomaly. The difference in the 2020 emissions

295 of BC during the lockdown from the respective emissions in the same period in each of the

296 previous years (2015–2019) is illustrated in Supplementary Figure 1.

297 Overall, BC emissions decreased by ~48 kt during the COVID-19 lockdown in the

298 inversion domain. We record a significant decrease in BC emissions in Central Europe

299 (Northern Italy, Austria, Germany, Spain and some Balkan countries) (Figure 5) compared to

300 the same period during the last five years. On average, emissions declined from 44 to 39 kt over

301 Europe. The decrease has the same characteristics when compared to each of previous years

302 since 2015 (Supplementary Figure 1) based on measurements of BC at the same stations as

303 those used for the 2020 inversion. The countries that showed drastic reductions in BC emissions

304 were those that suffered from the pandemic dramatically, with many human losses, strict social

305 distancing rules and consequently less transport. Specifically, emissions dropped by 20% in

306 Italy (2.4 to 2.0 kt), 40% in Germany (2.2 to 1.3 kt), 23% in Spain (3.4 to 2.6 kt) and remained

307 the same or were slightly enhanced in Poland (~7.0 kt), France (~2.2 kt) and Scandinavia (~1.2

308 kt). Overall, BC emissions in Western Europe declined by 22% (6.2 to 4.8 kt), in Southern

309 Europe by 36% (12 to 7.7 kt) and in Northern Europe by 26% (3.8 to 2.8 kt). BC emissions in

310 Eastern Europe were slightly increased during the 2020 lockdown as compared to the same

311 period in the last five years (22 to 24 kt). Note that these numbers correspond to BC emissions

312 during the COVID-19 lockdown period only (mid-March – April 2020).

313 Some localised areas of increased BC emissions exist in Southern France, Belgium,

314 Northern Germany and Eastern Europe (Figure 5), which are observed relative to almost every

315   year since 2015 (Supplementary Figure 1). While some hotspots in France cannot be easily

316   explained, increased emissions in Eastern European countries are likely due to increased

317   residential combustion, as people had to stay home during the lockdown. The combination of

318   the financial consequences of the COVID-19 lockdown with the relatively low GDP per capita

319   in these countries and the fact that from mid-March to end of April 2020 surface temperatures

320   in these countries were significantly lower than in previous years is suggestive of increased

321   emissions due to residential combustion. This source is most important in Eastern Europe

322   (Klimont et al., 2017). Although residential combustion can be performed for heating or

323   cooking needs in poorer countries, it is also believed to provide a more natural type of warmth

324   and a comfortable and relaxing environment. Hence, it should not be assumed as an emission

325   source in countries with lower GDPs only, especially as people spent more time at home.

326   Moreover, the prevailing average temperatures over Europe during the lockdown were below

327   15°C (Supplementary Figure 2), a temperature used as a basis temperature below which

328   residential combustion increases (Quayle and Diaz, 1980; Stohl et al., 2013).

3.3   Uncertainty and validation of the posterior emissions

330   One of the basic problems when dealing with inverse modelling is that changing model,

331   observational, or prior uncertainties can have drastic impacts on posterior emissions. We

332   addressed this issue by finding the optimal parameters, in order to have a reduced χ^2 statistic

333   around unity (see section 2.3). However, there are two other sources of uncertainty that,

334   although not linked with the inversion algorithm, could affect posterior emissions drastically.

335   The first is the use of different prior emissions; to estimate this type of uncertainty, we

336   performed five inversions using each of the prior emission datasets (ECLIPSEv6 and v5,

337   EDGAR_HTAPv2.2, ACCMIPv5 and PKU). The uncertainty was calculated as the gridded

338   standard deviation of the posterior emissions resulting from the five inversions. The second

339   type of uncertainty concerns measurement of BC, which is defined as a function of five

340   properties (Petzold et al., 2013). However, as of today, no single instrument exists that could

341   measure all of these properties at the same time. Hence, BC is not a single particle conistuent,

342   rather an operational definition depending on the measurement technique (Petzold et al., 2013).

343   Here we use light absorption coefficients (Petzold et al., 2013) converted to equivalent BC

344   (eBC) using the mass absorption cross section (MAC). The MAC is instrument specific and

345   wavelength dependent. The site-specific MAC values used to convert the filter-based light

346   absorption to eBC can be seen in Table 1. It has been reported that MAC values vary from 2 –

347   3 m^2 g^{-1} up to 20 m^2 g^{-1} (Bond and Bergstrom, 2006). To estimate the uncertainty of the posterior

348   fluxes associated with the variable MAC, we performed a sensitivity study using MAC values

349   of 5, 10 and 20 m^2 g^{-1} in all stations, as well as variable MAC values for each stations (Table

350   1). Since these values are lognormally distributed, the uncertainty is calculated as the geometric

351   standard deviation. The impact of other sources of uncertainty, such as those referring to

352   scavenging coefficients, particle size and density that are used in the model have been studied

353   before (Evangeliou et al., 2018; Grythe et al., 2017).

354   The posterior emissions are less sensitive to the use of different MACs than the use of

355   different prior inventories (Figure 6). The relative uncertainty due to different use of MAC

356   values was up to 20–30% in most of Europe and increases dramatically far from the

357   observations. Accordingly, the emission uncertainty of BC from the use of different priors was

358   estimated to be up to 40% in Europe and shows very similar characteristics (same hot-spot

359   regions and larger values where measurements lack). Overall, the combined uncertainty of BC

360   emissions was ~60% in Europe.

361   Validation of top-down emissions obtained by inversion algorithms can be proper only if

362   measurements that were not included in the inversion are to be used (independent observations).

363   For this reason, we left out of the inversion observations from two stations (DE0054K and

364   DE0066R, Table 1). Due to the higher measurement station density in Central Europe, we

365   randomly selected two German stations, rather than from a country that is adjacent to regions

366   that lack observations.

367   The prior, optimized and measured concentrations are shown in Figure 7 together with

368   MERRA-2 surface BC concentrations at the same stations. The average footprint emission

369   sensitivities are also given for the period of the lockdown. At station DE0054K, prior emissions

370   represent observations very well until the beginning of the lockdown and then fail (Figure 7).

371   On the other hand, the posterior emissions represent the variant concentrations during the

372   lockdown effectively and also manage to capture some concentration peaks, which is reflected

373   by lower $nRMSE$. Backward modelling showed that the enhanced concentrations originate

374   from Northern Germany and the Netherlands, where posterior emissions were increased

375   compared with the prior ones (Figure 4). A similar pattern was seen at station DE0066K,

376   although this station showed concentrations up to 4 mg m^{-3} (Figure 7). Again, the optimized

377   emissions managed to represent the peaks at the end of January 2020 and at the beginning of

378   the lockdown, which is again reflected by a half $nRMSE$ values and MFB close to zero as

379   compared to the priors. The larger concentrations during the lockdown result from increased

380   emissions over Eastern Germany, Poland and the Netherlands, as well as in oil industries in the

381   North Sea (Figure 4b). In all these regions the footprint emissions sensitivities corresponding

382   to the two independent stations were the highest.

4 Discussion

383

384   The improved air quality that Europe experienced during the lockdown was also evident

385   from the assimilated MERRA-2 satellite-based BC data. The latter are plotted in Supplementary

386   Figure 3 (left axis), together with the posterior emissions calculated in the present study (right

387   axis) between 2015–2020. Many of the ACTRIS stations reported increased light absorption in

388   the beginning of the lockdown (e.g., Figure 7); MERRA-2 data show the same patterns in

389   France, Italy, UK and in Spain, and in all of Europe, in general. This can be explained by

390   residential combustion considering that the surface temperature during the lockdown was lower

391   than in previous years (Figure 5). The latter was confirmed by MERRA-2 reanalysis Ångström

392   Exponent (AE) parameter at 470–870 nm, which shows higher values over Central and Eastern

393   Europe during the lockdown in 2020 than in the same period of the previous years (Figure 8a,b).

394   Larger AE values confirm the presence of wood burning aerosols (Eck et al., 1999). The fact

395   that during the COVID-19 lockdown, residential combustion was a significant aerosol source

396   in Europe, as compared to the previous years, was also confirmed by real-time observations of

397   absorption AE from the AERONET data in five selected stations over Europe (Figure 8c).

398   Measured absorption AE was higher during mid-March to April 2020 than in the same period

399   of the last five years.

400   Emissions of BC calculated with Bayesian inversion for the lockdown period dropped

401   substantially in most of the countries that suffered from further spread of the virus and,

402   accordingly, from strict lockdown measures, as compared to the respective emissions in the

403   beginning of 2020 (Supplementary Figure 3). Specifically, the decrease in France was as high

404   as 40%, 11% in Italy, 32% in Germany, 15% in Spain and 25% in the UK. Emissions also

405   declined in Scandinavia by 12%, although Sweden did not enforce a lockdown. Overall, a

406   reduction in BC emissions of about 10% can be concluded for Europe as a whole due to the

407   lockdown. Stronger decreases in Eastern Europe were likely partly compensated by increased

408   residential combustion in resulting from the prevailing low temperatures.

409   We report a decrease of 11% in BC emissions in Europe during the lockdown that resulted

410   from the COVID-19 outbreak, as compared to the same period in all previous years since 2015,

411   based on particle light absorption measurements. We highlight these changes in BC emissions

412   as a result of COVID-19 restrictions by plotting the temporal variability of the BC emissions

413   in the 5 previous years (2015 – 2019) for France, Italy, Germany, Spain, Scandinavia and

414   Europe (Figure 9). We record a decrease in emissions of BC in France, Italy, Germany and

415   Scandinavia in mid-March to April 2020, opposite to what was estimated for all years between

416   2015 and 2019, which is obviously due to COVID-19. The UK and Spain showed a similar

417   decrease in mid-March to April emissions in all previous years (2015–2019). However, the

418   estimated posterior BC emissions during the 2020 lockdown were significantly lower than those

419   of the same period in any of the previous years. Overall, emissions declined by 20% in Italy,

420   40% in Germany, 23% in Spain and remained the same in France and slightly enhanced in

421   Scandinavia as compared to those of the last five years.

5   Conclusions

423   The impact of the COVID-19 lockdowns over Europe on the BC emissions, in response

424   to the pandemic was assessed in the present manuscript. Particle light absorption measurements

425   from 17 ACTRIS stations all around Europe were rapidly gathered and cleaned to produce a

426   high-quality product. The latter was used in a well-established Bayesian inversion framework

427   and BC emissions were optimised over Europe to better capture the observations. We calculate

428   that the optimised (posterior) BC emissions declined from 44 to 39 kt (11%) during the

429   lockdown over Europe, as compared to the same period in the previous five years (2015–2019).

430   The largest reductions were calculated for countries that suffered from the pandemic

431   dramatically, such as Italy (from 2.4 to 2.0 kt), Germany (from 2.2 to 1.3 kt), Spain (from 3.4

432   to 2.6 kt). BC emissions in Western Europe during the 2020 lockdown were decreased from 6.2

433   to 4.8 kt (22%), in Southern Europe from 12 to 7.7 kt (36%) and in Northern Europe from 3.8

434   to 2.8 kt (26%) as compared to the same period in the last five years. BC emissions were slightly

435   enhanced in Eastern Europe (from 22 to 24 kt) during the lockdown, due to increased residential

436   combustion, as people had to stay home and temperatures at that time were the lowest of the

437   last five years. The presence of wood burning aerosols during the lockdowns was confirmed by

438   large MERRA-2 AE, as well as from absorption AE measurements from AERONET that were

439   higher in the lockdowns than in the same period of the last five years. The impact of the

440   European lockdowns on BC emissions was also confirmed by a 10% decrease of the posterior

441   emissions over Europe in the beginning of the lockdown, as compared to the period before,

442   opposite to what was calculated in the previous years, which is obviously due to COVID-19.

443   This decrease was more pronounced in France (40%), Italy (11%), Germany (32%), Spain

444   (15%), UK (25%) and in Scandinavian countries (12%). The full impact of the disastrous

445   pandemic will likely take years to assess. Nevertheless, with COVID-19 cases once again

446   increasing in many countries, the information presented here are essential to understand the full

447   health and climate impacts of lockdown measures.

448   *Data availability.* All measurement data and model outputs used for the present publication are

449   open and can be downloaded from https://doi.org/10.21336/gen.b5vj-sn33 or upon request to

450   the corresponding author. All prior emission datasets are also available for download. ECLIPSE

451   emissions   can   be   obtained   from

452   http://www.iiasa.ac.at/web/home/research/researchPrograms/air/Global_emissions.html,

453   EDGAR version HTAP_V2.2 from http://edgar.jrc.ec.europa.eu/methodology.php#, ACCMIP

454   version 5 from http://accent.aero.jussieu.fr/ACCMIP_metadata.php) and PKU from

455   http://inventory.pku.edu.cn. FLEXPART is open in public and can be downloaded from

456   https://www.flexpart.eu, so as FLEXINVERT+ from https://flexinvert.nilu.no. MERRA-2 re-

457   analysis data can be obtained from https://disc.gsfc.nasa.gov, so as AERONET measurements

458   from https://aeronet.gsfc.nasa.gov.

459   *Author contributions.* N.E. led the work and wrote the paper. S.E. and A.S. commented on the

460   inversion framework. C.L.M., P.L., L.A.A., J.B., B.T.B., M.F., H.F., M.P., J.Y.D., N.P., J.P.P.,

461   K.S., M.S., K.E., S.V. and A.W. provided the ACTRIS measurements. S.M.P. gave

462   recommendations on the mac values used and wrote parts of the paper. All authors gave input

463   in the writing process.

464   *Competing interests.* The authors declare no competing interests.

465   *Acknowledgements.* This study was supported by the Research Council of Norway (project ID:

466   275407, COMBAT – Quantification of Global Ammonia Sources constrained by a Bayesian

467   Inversion Technique). N.E. and S.E. received funding from Arctic Monitoring & Assessment

468   Programme (AMAP). J.B. was supported by the Academy of Finland project Novel Assessment

469   of Black Carbon in the Eurasian Arctic: From Historical Concentrations and Sources to Future

470   Climate Impacts (NABCEA, project number 296302), and the Academy of Finland Centre of

471   Excellence program (project number 307331) and COST Action CA16109 Chemical On-Line

472   cOmpoSition and Source Apportionment of fine aerosoL, COLOSSAL. We thank B.

473   Mougenot, O. Hagolle, A. Chaikovsky, P. Goloub, J. Lorente, R. Becker and M. Wiegner for

474   their effort in establishing and maintaining the AERONET sites Ben Salem (Tunisia), Minsk

475   (Belarus), Montsec (Spain), MetObs Lindenberg (Germany) and Munich University

476   (Germany). The research leading to the ACTRIS measurements has received funding from the

477   European Union's Horizon 2020 research and innovation programme under grant agreement

478   No 654109 and the Cloudnet project (European Union contract EVK2-2000-00611).

479

References

481   Ackerman, a. S.: Reduction of Tropical Cloudiness by Soot, Science (80-.)., 288(5468),
482   1042–1047, doi:10.1126/science.288.5468.1042, 2000.
483   Adams, M. D.: Air pollution in Ontario, Canada during the COVID-19 State of Emergency,
484   Sci. Total Environ., 742, 140516, doi:10.1016/j.scitotenv.2020.140516, 2020.
485   Bauwens, M., Compernolle, S., Stavrakou, T., Müller, J. F., van Gent, J., Eskes, H., Levelt, P.
486   F., van der A, R., Veefkind, J. P., Vlietinck, J., Yu, H. and Zehner, C.: Impact of Coronavirus
487   Outbreak on NO2 Pollution Assessed Using TROPOMI and OMI Observations, Geophys.
488   Res. Lett., 47(11), 1–9, doi:10.1029/2020GL087978, 2020.
489   Berman, J. D. and Ebisu, K.: Changes in U.S. air pollution during the COVID-19 pandemic,
490   Sci. Total Environ., 739, 139864, doi:10.1016/j.scitotenv.2020.139864, 2020.
491   Bond, T. C. and Bergstrom, R. W.: Light Absorption by Carbonaceous Particles: An
492   Investigative Review, Aerosol Sci. Technol., 40(1), 27–67, doi:10.1080/02786820500421521,
493   2006.
494   Bond, T. C., Doherty, S. J., Fahey, D. W., Forster, P. M., Berntsen, T., Deangelo, B. J.,
495   Flanner, M. G., Ghan, S., Kärcher, B., Koch, D., Kinne, S., Kondo, Y., Quinn, P. K., Sarofim,
496   M. C., Schultz, M. G., Schulz, M., Venkataraman, C., Zhang, H., Zhang, S., Bellouin, N.,
497   Guttikunda, S. K., Hopke, P. K., Jacobson, M. Z., Kaiser, J. W., Klimont, Z., Lohmann, U.,
498   Schwarz, J. P., Shindell, D., Storelvmo, T., Warren, S. G. and Zender, C. S.: Bounding the
499   role of black carbon in the climate system: A scientific assessment, J. Geophys. Res. Atmos.,
500   118(11), 5380–5552, doi:10.1002/jgrd.50171, 2013.
501   Buchard, V., Randles, C. A., da Silva, A. M., Darmenov, A., Colarco, P. R., Govindaraju, R.,
502   Ferrare, R., Hair, J., Beyersdorf, A. J., Ziemba, L. D. and Yu, H.: The MERRA-2 aerosol
503   reanalysis, 1980 onward. Part II: Evaluation and case studies, J. Clim., 30(17), 6851–6872,
504   doi:10.1175/JCLI-D-16-0613.1, 2017.
505   Cassiani, M., Stohl, A. and Brioude, J.: Lagrangian Stochastic Modelling of Dispersion in the
506   Convective Boundary Layer with Skewed Turbulence Conditions and a Vertical Density
507   Gradient: Formulation and Implementation in the FLEXPART Model, Boundary-Layer
508   Meteorol., 154(3), 367–390, doi:10.1007/s10546-014-9976-5, 2014.
509   Clarke, A. D. and Noone, K. J.: Soot in the arctic snowpack: a cause for perturbations in
510   radiative transfer, Atmos. Environ., 41(SUPPL.), 64–72, doi:10.1016/0004-6981(85)90113-1,
511   1985.
512   Conticini, E., Frediani, B. and Caro, D.: Can atmospheric pollution be considered a co-factor
513   in extremely high level of SARS-CoV-2 lethality in Northern Italy?, Environ. Pollut., 261,
514   114465, doi:10.1016/j.envpol.2020.114465, 2020.
515   Copernicus Climate Change Service (C3S): C3S ERA5-Land reanalysis . Copernicus Climate
516   Change Service, [online] Available from: https://cds.climate.copernicus.eu/cdsapp#!/home
517   (Accessed 31 August 2020), 2020.
518   Dantas, G., Siciliano, B., França, B. B., da Silva, C. M. and Arbilla, G.: The impact of
519   COVID-19 partial lockdown on the air quality of the city of Rio de Janeiro, Brazil, Sci. Total
520   Environ., 729, doi:10.1016/j.scitotenv.2020.139085, 2020.
521   Diffenbaugh, N. S., Field, C. B., Appel, E. A., Azevedo, I. L., Baldocchi, D. D., Burke, M.,
522   Burney, J. A., Ciais, P., Davis, S. J., Fiore, A. M., Fletcher, S. M., Hertel, T. W., Horton, D.
523   E., Hsiang, S. M., Jackson, R. B., Jin, X., Levi, M., Lobell, D. B., McKinley, G. A., Moore, F.

524   C., Montgomery, A., Nadeau, K. C., Pataki, D. E., Randerson, J. T., Reichstein, M., Schnell,
525   J. L., Seneviratne, S. I., Singh, D., Steiner, A. L. and Wong-Parodi, G.: The COVID-19
526   lockdowns: a window into the Earth System, Nat. Rev. Earth Environ., 1–12,
527   doi:10.1038/s43017-020-0079-1, 2020.

528   Dutheil, F., Baker, J. S. and Navel, V.: COVID-19 as a factor influencing air pollution?,
529   Environ. Pollut., 263, 2019–2021, doi:10.1016/j.envpol.2020.114466, 2020.

530   Eck, T. F., Holben, B. N., Reid, J. S., Smirnov, A., Neill, N. T. O., Slutsker, I. and Kinne, S.:
531   Wavelength dependence of the optical depth of biomass burning, urban, and desert dust
532   aerosols, J. Geophys. Res., 104(D24), 31333–31349, 1999.

533   Evangeliou, N., Thompson, R. L., Eckhardt, S. and Stohl, A.: Top-down estimates of black
534   carbon emissions at high latitudes using an atmospheric transport model and a Bayesian
535   inversion framework, Atmos. Chem. Phys., 18(20), doi:10.5194/acp-18-15307-2018, 2018.

536   Forster, C., Stohl, A. and Seibert, P.: Parameterization of convective transport in a Lagrangian
537   particle dispersion model and its evaluation, J. Appl. Meteorol. Climatol., 46(4), 403–422,
538   doi:10.1175/JAM2470.1, 2007.

539   Giglio, L., Randerson, J. T. and van der Werf, G. R.: Analysis of daily, monthly, and annual
540   burned area using the fourth-generation global fire emissions database (GFED4), J. Geophys.
541   Res. Biogeosciences, 118, 317–328, doi:10.1002/jgrg.20042, 2013, 2013.

542   Grythe, H., Kristiansen, N. I., Groot Zwaaftink, C. D., Eckhardt, S., Ström, J., Tunved, P.,
543   Krejci, R. and Stohl, A.: A new aerosol wet removal scheme for the Lagrangian particle
544   model FLEXPARTv10, Geosci. Model Dev., 10, 1447–1466, doi:10.5194/gmd-10-1447-
545   2017, 2017.

546   Gueymard, C. A. and Yang, D.: Worldwide validation of CAMS and MERRA-2 reanalysis
547   aerosol optical depth products using 15 years of AERONET observations, Atmos. Environ.,
548   225(November 2019), 117216, doi:10.1016/j.atmosenv.2019.117216, 2020.

549   He, G., Pan, Y. and Tanaka, T.: The short-term impacts of COVID-19 lockdown on urban air
550   pollution in China, Nat. Sustain., doi:10.1038/s41893-020-0581-y, 2020.

551   Hegg, D. A., Warren, S. G., Grenfell, T. C., Doherty, S. J., Larson, T. V. and Clarke, A. D.:
552   Source attribution of black carbon in arctic snow, Environ. Sci. Technol., 43(11), 4016–4021,
553   doi:10.1021/es803623f, 2009.

554   Holben, B. N., Eck, T. F., Slutsker, I., Tanré, D., Buis, J. P., Setzer, A., Vermote, E., Reagan,
555   J. A., Kaufman, Y. J., Nakajima, T., Lavenu, F., Jankowiak, I. and Smirnov, A.:
556   AERONET—A Federated Instrument Network and Data Archive for Aerosol
557   Characterization, Remote Sens. Environ., 66(1), 1–16, doi:10.1016/S0034-4257(98)00031-5,
558   1998.

559   Huang, C., Wang, Y., Li, X., Ren, L., Zhao, J., Hu, Y., Zhang, L., Fan, G., Xu, J., Gu, X.,
560   Cheng, Z., Yu, T., Xia, J., Wei, Y., Wu, W., Xie, X., Yin, W., Li, H., Liu, M., Xiao, Y., Gao,
561   H., Guo, L., Xie, J., Wang, G., Jiang, R., Gao, Z., Jin, Q., Wang, J. and Cao, B.: Clinical
562   features of patients infected with 2019 novel coronavirus in Wuhan, China, Lancet,
563   395(10223), 497–506, doi:10.1016/S0140-6736(20)30183-5, 2020.

564   Janssens-Maenhout, G., Crippa, M., Guizzardi, D., Dentener, F., Muntean, M., Pouliot, G.,
565   Keating, T., Zhang, Q., Kurokawa, J., Wankmüller, R., Denier Van Der Gon, H., Kuenen, J. J.
566   P., Klimont, Z., Frost, G., Darras, S., Koffi, B. and Li, M.: HTAP-v2.2: A mosaic of regional
567   and global emission grid maps for 2008 and 2010 to study hemispheric transport of air
568   pollution, Atmos. Chem. Phys., 15(19), 11411–11432, doi:10.5194/acp-15-11411-2015, 2015.

569   Jinhuan, Q. and Liquan, Y.: Variation characteristics of atmospheric aerosol optical depths
570   and visibility in North China during 1980 } 1994, Atmos. Environ., 34, 603–609, 2000.

571   John Hopkins University of Medicine: Coronavirus resource center, [online] Available from:
572   https://coronavirus.jhu.edu/map.html (Accessed 10 August 2020), 2020.

573   Kerimray, A., Baimatova, N., Ibragimova, O. P., Bukenov, B., Kenessov, B., Plotitsyn, P. and

574   Karaca, F.: Assessing air quality changes in large cities during COVID-19 lockdowns: The
575   impacts of traffic-free urban conditions in Almaty, Kazakhstan, Sci. Total Environ., 730,
576   139179, doi:10.1016/j.scitotenv.2020.139179, 2020.
577   Klimont, Z., Kupiainen, K., Heyes, C., Purohit, P., Cofala, J., Rafaj, P., Borken-Kleefeld, J.
578   and Schöpp, W.: Global anthropogenic emissions of particulate matter including black
579   carbon, Atmos. Chem. Phys., 17, 8681–8723, doi:10.5194/acp-17- 50 8681-2017, 2017.
580   Kummu, M., Taka, M. and Guillaume, J. H. A.: Data from: Gridded global datasets for Gross
581   Domestic Product and Human Development Index over 1990-2015, v2, Dryad, Dataset,
582   doi:https://doi.org/10.5061/dryad.dk1j0, 2020.
583   Lack, D. A. and Langridge, J. M.: On the attribution of black and brown carbon light
584   absorption using the Ångström exponent, Atmos. Chem. Phys., 13(20), 10535–10543,
585   doi:10.5194/acp-13-10535-2013, 2013.
586   Laj, P., Bigi, A., Rose, C., Andrews, E., Lund Myhre, C., Collaud Coen, M., Wiedensohler,
587   A., Schultz, M., Ogren, J., Fiebig, M., Gliß, J., Mortier, A., Pandolfi, M., Petäjä, T., Kim, S.-
588   W., Aas, W., Putaud, J.-P., Mayol-Bracero, O., Keywood, M., Labrador, L., Aalto, P.,
589   Ahlberg, E., Alados Arboledas, L., Alastuey, A., Andrade, M., Artíñano, B., Ausmeel, S.,
590   Arsov, T., Asmi, E., Backman, J., Baltensperger, U., Bastian, S., Bath, O., Beukes, J. P.,
591   Brem, B., Bukowiecki, N., Conil, S., Couret, C., Day, D., Dayantolis, W., Degorska, A., Dos
592   Santos, S. M., Eleftheriadis, K., Fetfatzis, P., Favez, O., Flentje, H., Gini, M., Gregorič, A.,
593   Gysel-Beer, M., Hallar, G., Hand, J., Hoffer, A., Hueglin, C., Hooda, R., Hyvärinen, A.,
594   Kalapov, I., Kalivitis, N., Kasper-Giebl, A., Kim, J. E., Kouvarakis, G., Kranjc, I., Krejci, R.,
595   Kulmala, M., Labuschagne, C., Lee, H.-J., Lihavainen, H., Lin, N.-H., Löschau, G., Luoma,
596   K., Marinoni, A., Meinhardt, F., Merkel, M., Metzger, J.-M., Mihalopoulos, N., Nguyen, N.
597   A., Ondracek, J., Peréz, N., Perrone, M. R., Petit, J.-E., Picard, D., Pichon, J.-M., Pont, V.,
598   Prats, N., Prenni, A., Reisen, F., Romano, S., Sellegri, K., Sharma, S., Schauer, G., Sheridan,
599   P., Sherman, J. P., Schütze, M., Schwerin, A., Sohmer, R., Sorribas, M., Steinbacher, M.,
600   Sun, J., Titos, G., Tokzko, B., et al.: A global analysis of climate-relevant aerosol properties
601   retrieved from the network of GAW near-surface observatories, Atmos. Meas. Tech. Discuss.,
602   1–70, doi:10.5194/amt-2019-499, 2020.
603   Lamarque, J. F., Shindell, D. T., Josse, B., Young, P. J., Cionni, I., Eyring, V., Bergmann, D.,
604   Cameron-Smith, P., Collins, W. J., Doherty, R., Dalsoren, S., Faluvegi, G., Folberth, G.,
605   Ghan, S. J., Horowitz, L. W., Lee, Y. H., MacKenzie, I. A., Nagashima, T., Naik, V.,
606   Plummer, D., Righi, M., Rumbold, S. T., Schulz, M., Skeie, R. B., Stevenson, D. S., Strode,
607   S., Sudo, K., Szopa, S., Voulgarakis, A. and Zeng, G.: The atmospheric chemistry and climate
608   model intercomparison Project (ACCMIP): Overview and description of models, simulations
609   and climate diagnostics, Geosci. Model Dev., 6(1), 179–206, doi:10.5194/gmd-6-179-2013,
610   2013.
611   Le, T., Wang, Y., Liu, L., Yang, J., Yung, Y. L., Li, G. and Seinfeld, J. H.: Unexpected air
612   pollution with marked emission reductions during the COVID-19 outbreak in China, Science
613   (80-.)., (2), eabb7431, doi:10.1126/science.abb7431, 2020.
614   Lian, X., Huang, J., Huang, R., Liu, C., Wang, L. and Zhang, T.: Impact of city lockdown on
615   the air quality of COVID-19-hit of Wuhan city, Sci. Total Environ., 742, 140556,
616   doi:10.1016/j.scitotenv.2020.140556, 2020.
617   Long, C. M., Nascarella, M. A. and Valberg, P. A.: Carbon black vs. black carbon and other
618   airborne materials containing elemental carbon: Physical and chemical distinctions, Environ.
619   Pollut., 181, 271–286, doi:10.1016/j.envpol.2013.06.009, 2013.
620   Myhre, G., Samset, B. H., Schulz, M., Balkanski, Y., Bauer, S., Berntsen, T. K., Bian, H.,
621   Bellouin, N., Chin, M., Diehl, T., Easter, R. C., Feichter, J., Ghan, S. J., Hauglustaine, D.,
622   Iversen, T., Kinne, S., Kirkevåg, A., Lamarque, J. F., Lin, G., Liu, X., Lund, M. T., Luo, G.,
623   Ma, X., Van Noije, T., Penner, J. E., Rasch, P. J., Ruiz, A., Seland, Skeie, R. B., Stier, P.,

624   Takemura, T., Tsigaridis, K., Wang, P., Wang, Z., Xu, L., Yu, H., Yu, F., Yoon, J. H., Zhang,
625   K., Zhang, H. and Zhou, C.: Radiative forcing of the direct aerosol effect from AeroCom
626   Phase II simulations, Atmos. Chem. Phys., 13(4), 1853–1877, doi:10.5194/acp-13-1853-2013,
627   2013.
628   Otmani, A., Benchrif, A., Tahri, M., Bounakhla, M., Chakir, E. M., El Bouch, M. and
629   Krombi, M.: Impact of Covid-19 lockdown on PM10, SO2 and NO2 concentrations in Salé
630   City (Morocco), Sci. Total Environ., 735(2), 139541, doi:10.1016/j.scitotenv.2020.139541,
631   2020.
632   Petzold, A., Ogren, J. A., Fiebig, M., Laj, P., Li, S. M., Baltensperger, U., Holzer-Popp, T.,
633   Kinne, S., Pappalardo, G., Sugimoto, N., Wehrli, C., Wiedensohler, A. and Zhang, X. Y.:
634   Recommendations for reporting black carbon measurements, Atmos. Chem. Phys., 13(16),
635   8365–8379, doi:10.5194/acp-13-8365-2013, 2013.
636   Pisso, I., Sollum, E., Grythe, H., Kristiansen, N., Cassiani, M., Eckhardt, S., Arnold, D.,
637   Morton, D., Thompson, R. L., Groot Zwaaftink, C. D., Evangeliou, N., Sodemann, H.,
638   Haimberger, L., Henne, S., Brunner, D., Burkhart, J. F., Fouilloux, A., Brioude, J., Philipp,
639   A., Seibert, P. and Stohl, A.: The Lagrangian particle dispersion model FLEXPART version
640   10.4, Geosci. Model Dev., 12, 4955–4997, doi:10.5194/gmd-12-4955-2019, 2019.
641   Qin, W., Zhang, Y., Chen, J., Yu, Q., Cheng, S., Li, W., Liu, X. and Tian, H.: Variation,
642   sources and historical trend of black carbon in Beijing, China based on ground observation
643   and MERRA-2 reanalysis data, Environ. Pollut., 245(2), 853–863,
644   doi:10.1016/j.envpol.2018.11.063, 2019.
645   Quayle, R. G. and Diaz, H. F.: Heating degree day data applied to residential heating energy
646   consumption, J. Appl. Meteorol., 19, 241–246, 1980.
647   Le Quéré, C., Jackson, R. B., Jones, M. W., Smith, A. J. P., Abernethy, S., Andrew, R. M.,
648   De-Gol, A. J., Willis, D. R., Shan, Y., Canadell, J. G., Friedlingstein, P., Creutzig, F. and
649   Peters, G. P.: Temporary reduction in daily global CO2 emissions during the COVID-19
650   forced confinement, Nat. Clim. Chang., 10(7), 647–653, doi:10.1038/s41558-020-0797-x,
651   2020.
652   Randles, C. A., da Silva, A. M., Buchard, V., Colarco, P. R., Darmenov, A., Govindaraju, R.,
653   Smirnov, A., Holben, B., Ferrare, R., Hair, J., Shinozuka, Y. and Flynn, C. J.: The MERRA-2
654   aerosol reanalysis, 1980 onward. Part I: System description and data assimilation evaluation,
655   J. Clim., 30(17), 6823–6850, doi:10.1175/JCLI-D-16-0609.1, 2017.
656   Sicard, P., De Marco, A., Agathokleous, E., Feng, Z., Xu, X., Paoletti, E., Rodriguez, J. J. D.
657   and Calatayud, V.: Amplified ozone pollution in cities during the COVID-19 lockdown, Sci.
658   Total Environ., 735, doi:10.1016/j.scitotenv.2020.139542, 2020.
659   Sohrabi, C., Alsafi, Z., O'Neill, N., Khan, M., Kerwan, A., Al-Jabir, A., Iosifidis, C. and
660   Agha, R.: World Health Organization declares global emergency: A review of the 2019 novel
661   coronavirus (COVID-19), Int. J. Surg., 76(February), 71–76, doi:10.1016/j.ijsu.2020.02.034,
662   2020.
663   Stohl, A., Forster, C., Frank, A., Seibert, P. and Wotawa, G.: Technical note: The Lagrangian
664   particle dispersion model FLEXPART version 6.2, Atmos. Chem. Phys., 5(9), 2461–2474,
665   doi:10.5194/acp-5-2461-2005, 2005.
666   Stohl, A., Kim, J., Li, S., O'Doherty, S., Salameh, P. K., Saito, T., Vollmer, M. K., Wan, D.,
667   Yao, B., Yokouchi, Y. and Zhou, L. X.: Hydrochlorofluorocarbon and hydrofluorocarbon
668   emissions in East Asia determined by inverse modeling, Atmos. Chem. Phys. Discuss., 10(2),
669   2089–2129, doi:10.5194/acpd-10-2089-2010, 2010.
670   Stohl, A., Klimont, Z., Eckhardt, S., Kupiainen, K., Shevchenko, V. P., Kopeikin, V. M. and
671   Novigatsky, A. N.: Black carbon in the Arctic: The underestimated role of gas flaring and
672   residential combustion emissions, Atmos. Chem. Phys., 13(17), 8833–8855, doi:10.5194/acp-
673   13-8833-2013, 2013.

674   Sun, E., Xu, X., Che, H., Tang, Z., Gui, K., An, L., Lu, C. and Shi, G.: Variation in MERRA-
675   2 aerosol optical depth and absorption aerosol optical depth over China from 1980 to 2017, J.
676   Atmos. Solar-Terrestrial Phys., 186(January), 8–19, doi:10.1016/j.jastp.2019.01.019, 2019.
677   Tarantola, A.: Inverse Problem Theory and Methods for Model Parameter Estimation, Society
678   for Industrial and Applied Mathematics, Philadelphia, Pa., 2005.
679   Thacker, W. C.: Data assimilation with inequality constraints, Ocean Model., 16(3–4), 264–
680   276, doi:10.1016/j.ocemod.2006.11.001, 2007.
681   Thompson, R. L. and Stohl, A.: FLEXINVERT: An atmospheric Bayesian inversion
682   framework for determining surface fluxes of trace species using an optimized grid, Geosci.
683   Model Dev., 7(5), 2223–2242, doi:10.5194/gmd-7-2223-2014, 2014.
684   Thompson, R. L., Stohl, A., Zhou, L. X., Dlugokencky, E., Fukuyama, Y., Tohjima, Y., Kim,
685   S. Y., Lee, H., Nisbet, E. G., Fisher, R. E., Lowry, D., Weiss, R. F., Prinn, R. G., O'Doherty,
686   S., Young, D. and White, J. W. C.: Methane emissions in East Asia for 2000-2011 estimated
687   using an atmospheric Bayesian inversion, J. Geophys. Res. Atmos., 120(9), 4352–4369,
688   doi:10.1002/2014JD022394, 2015.
689   Wang, P., Wang, H., Wang, Y. Q., Zhang, X. Y., Gong, S. L., Xue, M., Zhou, C. H., Liu, H.
690   L., An, X. Q., Niu, T. and Cheng, Y. L.: Inverse modeling of black carbon emissions over
691   China using ensemble data assimilation, Atmos. Chem. Phys., 16(2), 989–1002,
692   doi:10.5194/acp-16-989-2016, 2016.
693   Wang, R., Tao, S., Balkanski, Y., Ciais, P., Boucher, O., Liu, J., Piao, S., Shen, H., Vuolo, M.
694   R., Valari, M., Chen, H., Chen, Y., Cozic, A., Huang, Y., Li, B., Li, W., Shen, G., Wang, B.
695   and Zhang, Y.: Exposure to ambient black carbon derived from a unique inventory and high-
696   resolution model., Proc. Natl. Acad. Sci. U. S. A., 111(7), 2459–63,
697   doi:10.1073/pnas.1318763111, 2014a.
698   Wang, R., Tao, S., Shen, H., Huang, Y., Chen, H., Balkanski, Y., Boucher, O., Ciais, P.,
699   Shen, G., Li, W., Zhang, Y., Chen, Y., Lin, N., Su, S., Li, B., Liu, J. and Liu, W.: Trend in
700   global black carbon emissions from 1960 to 2007, Environ. Sci. Technol., 48(12), 6780–6787,
701   doi:10.1021/es5021422, 2014b.
702   WHO: Report of the WHO-China Joint Mission on Coronavirus Disease 2019 (COVID-19),
703   WHO-China Jt. Mission Coronavirus Dis. 2019, 2019(February), 16–24 [online] Available
704   from: https://www.who.int/docs/default-source/coronaviruse/who-china-joint-mission-on-
705   covid-19-final-report.pdf, 2020.
706   Zanatta, M., Gysel, M., Bukowiecki, N., M??ller, T., Weingartner, E., Areskoug, H., Fiebig,
707   M., Yttri, K. E., Mihalopoulos, N., Kouvarakis, G., Beddows, D., Harrison, R. M., Cavalli, F.,
708   Putaud, J. P., Spindler, G., Wiedensohler, A., Alastuey, A., Pandolfi, M., Sellegri, K.,
709   Swietlicki, E., Jaffrezo, J. L., Baltensperger, U. and Laj, P.: A European aerosol
710   phenomenology-5: Climatology of black carbon optical properties at 9 regional background
711   sites across Europe, Atmos. Environ., 145, 346–364, doi:10.1016/j.atmosenv.2016.09.035,
712   2016.
713   Zheng, H., Kong, S., Chen, N., Yan, Y., Liu, D., Zhu, B., Xu, K., Cao, W., Ding, Q., Lan, B.,
714   Zhang, Z., Zheng, M., Fan, Z., Cheng, Y., Zheng, S., Yao, L., Bai, Y., Zhao, T. and Qi, S.:
715   Significant changes in the chemical compositions and sources of PM2.5 in Wuhan since the
716   city lockdown as COVID-19, Sci. Total Environ., 739, doi:10.1016/j.scitotenv.2020.140000,
717   2020.
718   Zotter, P., Herich, H., Gysel, M., El-Haddad, I., Zhang, Y., Mocnik, G., Hüglin, C.,
719   Baltensperger, U., Szidat, S. and Prévôt, A. S. H.: Evaluation of the absorption Ångström
720   exponents for traffic and wood burning in the Aethalometer-based source apportionment
721   using radiocarbon measurements of ambient aerosol, Atmos. Chem. Phys., 17(6), 4229–4249,
722   doi:10.5194/acp-17-4229-2017, 2017.
723

724

TABLES & FIGURES

Table 1. Observation sites from the ACTRIS platform used to perform the inversions (dependent observations) and to validate the posterior emissions (independent observations) (the altitude indicates the sampling height in meters above sea level). Multi-Angle Absorption Photometers (MAAP) were used at all sites, except El Arenosillo (ES0100R) where a Continuous Light Absorption Photometer (CLAP) was used, Birkenes (NO0002R), where a Particle Soot Absorption Photometer (PSAP) and Observatoire Perenne de l' Environnement (FR0022R) and Zeppelin (NO0042G) where Aethalometers (AW31) were used.

Name	Latitude	Longitude	Altitude	Type	Wavelength (nm)	MAC$_{@637}$ (m^2 g^{-1})
Jungfraujoch (CH0001G)	46.55	7.99	3578	Dependent	637	10
Hohenpeissenberg (DE0043G)	47.80	11.01	985	Dependent	660	9.65
Melpitz (DE0044K)	51.53	12.93	86	Dependent	670	8.78
Zugspitze-Schneefernerhaus (DE0054R)	47.42	10.98	2671	Independent	670	9.51
Leipzig-Eisenbahnstrasse (DE0066K)	51.35	12.41	120	Independent	670	9.51
Izaña (ES0018G)	28.41	-16.50	2373	Dependent	670	9.51
Granada (ES0020U)	37.16	-3.61	680	Dependent	670	9.51
Montsec (ES0022R)	42.05	0.73	1571	Dependent	670	9.51
El Arenosillo (ES0100R)	37.10	-6.73	41	Dependent	652	13.64
Montseny (ES1778R)	41.77	2.35	700	Dependent	670	8.48
Pallas (FI0096G)	67.97	24.12	565	Dependent	637	10.00
Observatoire Perenne de l' Environnement (FR0022R)	48.56	5.51	392	Dependent	880	7.24
Puy de Dôme (FR0030R)	45.77	2.96	1465	Dependent	670	9.51
Ispra (IT0004R)	45.80	8.63	209	Dependent	880	6.96
Mt Cimone (IT0009R)	44.18	10.70	2165	Dependent	670	9.51
Birkenes II (NO0002R)	58.39	8.25	219	Dependent	660	7.59
Zeppelin mountain (NO0042G)	78.91	11.89	474	Dependent	880	7.24

735 **Table 2.** Statistical measures (***RMSE***, Pearson's R^2, ***MFB*** and ***nMAE***) for each of the prior

736 and posterior concentrations against dependent observations (observations that were used in the

737 inversion algorithm) for BC (eBC). Note that the inversion using ECLIPSEv6 prior emission

738 dataset gave the best agreement with the observations and therefore the results of this inversion

739 are presented here.

	nRMSE	Pearson's R^2	MFB	nMAE
Prior ECLIPSEv6	0.102	0.30	0.52	997
Prior ECLIPSEv5	0.098	0.18	-0.04	996
Prior EDGAR_HTAPv2.2	0.105	0.11	0.34	1017
Prior ACCMIPv5	0.101	0.28	0.36	971
Prior PKU	0.101	0.21	0.25	983
Posterior ECLIPSEv6	**0.073**	**0.60**	**0.03**	**714**
Posterior ECLIPSEv5	0.084	0.52	0.09	819
Posterior EDGAR_HTAPv2.2	0.084	0.53	0.20	815
Posterior ACCMIPv5	0.091	0.55	0.26	787
Posterior PKU	0.082	0.55	0.24	795

740
741
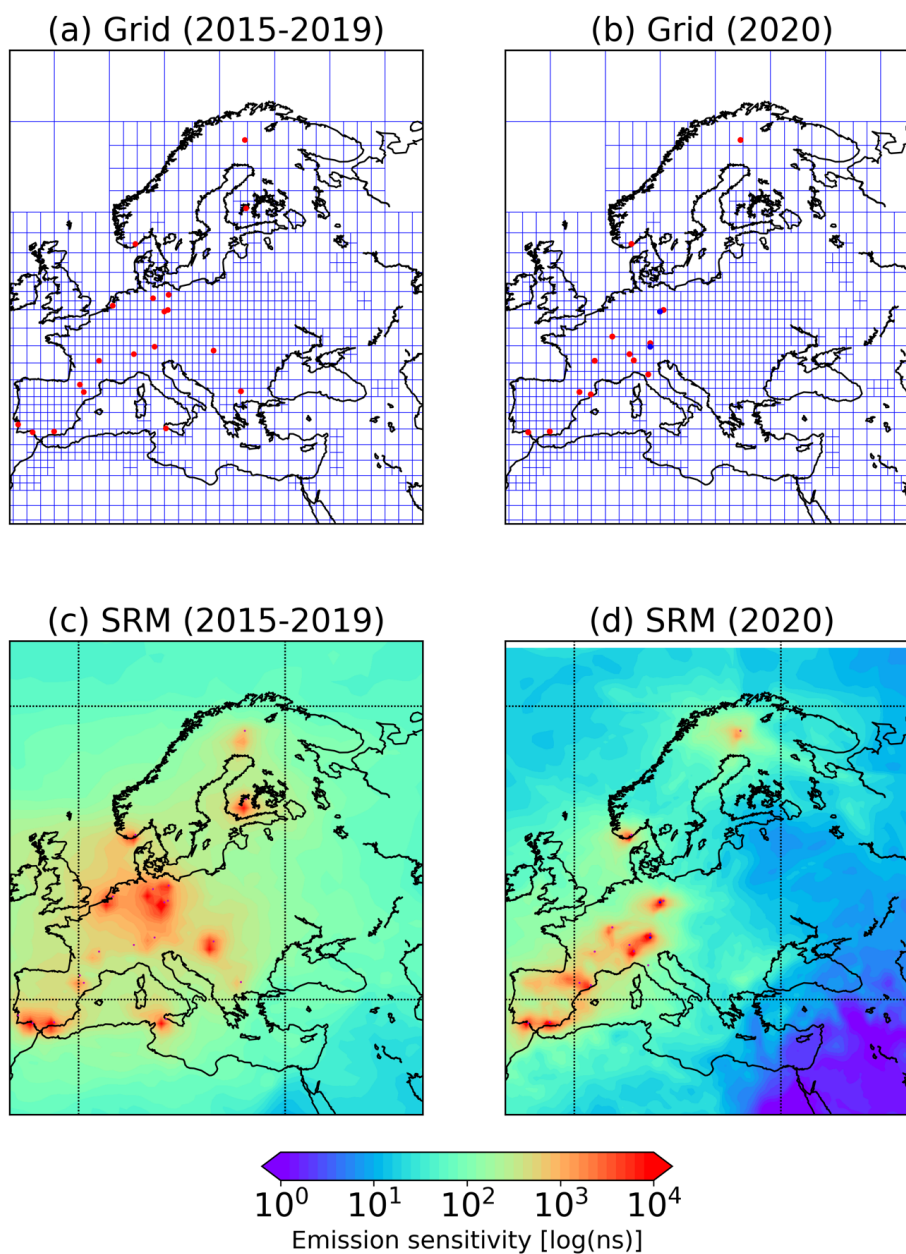
Figure 1. Aggregated inversion grid used for the (a) 2015–2019 and (b) 2020 inversions, respectively. The dependent measurements that were used in the inversion were taken from stations highlighted in red. The two independent stations that were used for the validation are shown in blue. (c, d) Footprint emission sensitivity (i.e. SRM) averaged over all observations and time steps for each of the inversions. Red points denote the location of each measurement site.

749
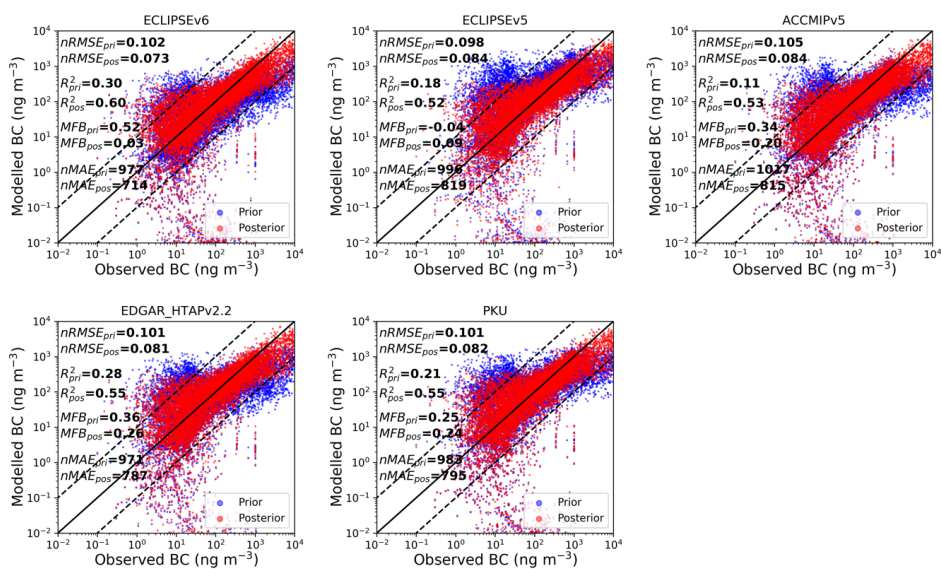
Figure 2. Scatter plots of prior and posterior concentrations against dependent observations (observations that were included in the inversion framework) from ACTRIS from January to April 2020. Four statistical measures (***nRMSE***, Pearson's R^2, ***MFB*** and ***nMAE***) were used to assess the performance of each inversion using five different prior emission inventories for BC (ECLIPSEv5, v6, ACCMIPv5, EDGAR_HTAPv2.2 and PKU).

755
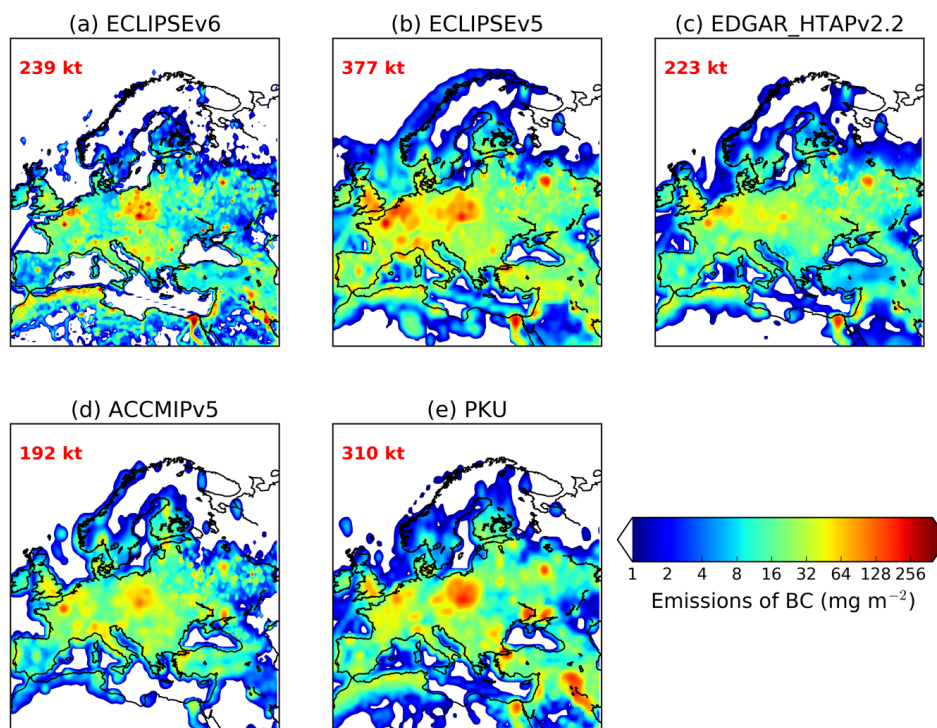
756
757 **Figure 3.** Prior emissions of black carbon (BC) used in the inversions. BC emissions from

758 anthropogenic sources were adopted from ECLIPSE version 5 and 6 (Evaluating the CLimate

759 and Air Quality ImPacts of ShortlivEd Pollutants) (Klimont et al., 2017), EDGAR (Emissions

760 Database for Global Atmospheric Research) version HTAP_v2.2 (Janssens-Maenhout et al.,

761 2015), ACCMIP (Emissions for Atmospheric Chemistry and Climate Model Intercomparison

762 Project) version 5 (Lamarque et al., 2013) and PKU (Peking University) (Wang et al., 2014b).

763 Biomass burning emissions of BC from Global Fire Emissions Database (GFED) version 4.1

764 (Giglio et al., 2013) were added in each of the aforementioned inventories.

765
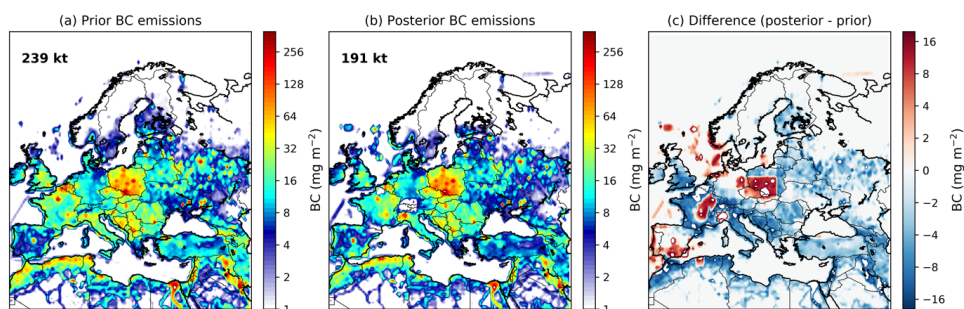
766
767 **Figure 4.** (a) Prior emissions of BC from ECLIPSEv6, (b) optimized (posterior) BC emissions

768 after processing the ACTRIS data into the inversion algorithm, and (c) difference between

769 posterior and prior emissions. All the results correspond to the inversion yielding the best results

770 (**Table 2** and **Figure 2**).

771

772
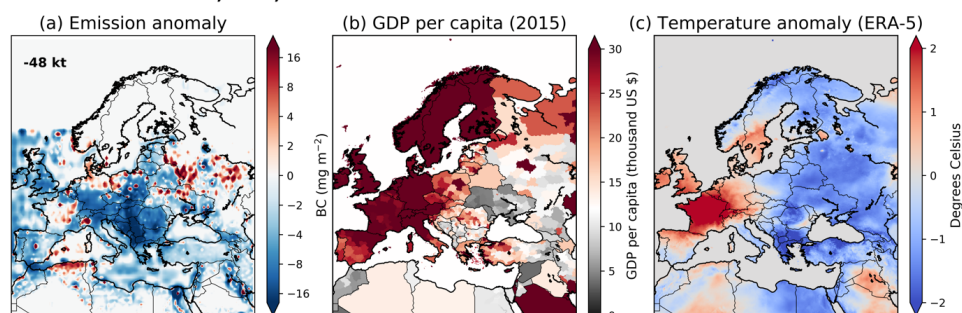
Figure 5. (a) Difference in posterior BC emissions during the lockdown (14 March to 30 April
2020) in Europe from the respective emissions during the same period in 2015 – 2019, (b) GDP
from Kummu et al. (2020), and (c) temperature anomaly from ERA-5 (Copernicus Climate
Change Service (C3S), 2020) for the same period as the emission anomaly. The base GDP value
below which a low income can be assumed was set to 12 thousand US dollars.

778
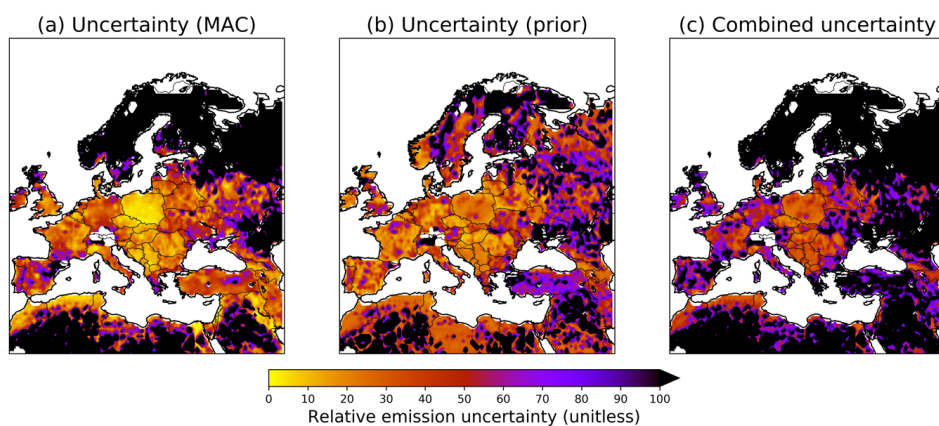
779
780 **Figure 6.** (a) Uncertainty of BC emissions due to the use of variable MAC values to convert

781 from aerosol absorption to eBC concentrations that are used by the inversion algorithm. (b)

782 Uncertainty due to the use of five different prior emissions inventories for BC. (c) Combined

783 uncertainty.

784
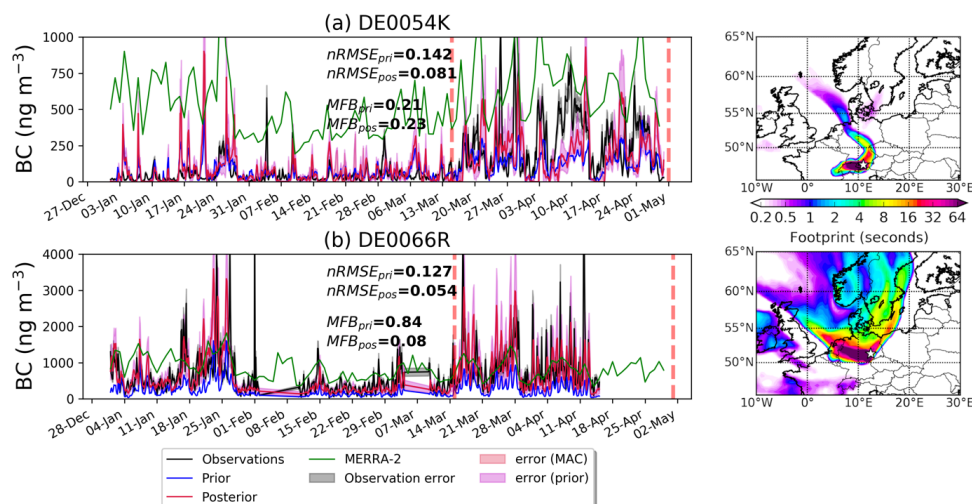
785
786 **Figure 7.** Prior and posterior BC concentrations at DE0054K and DE0066R stations that were

787 not included in the inversion are compared with observations. The validation is done by

788 calculating the *nRMSEs* and *MFBs* for the prior and posterior concentrations. The

789 uncertainty of the observations is also given together with the posterior uncertainties in the

790 concentrations calculated from the use of different MAC and prior emissions. For comparison,

791 we plot the concentrations from MERRA-2 at the same two stations. The vertical dashed lines

792 denote the period of the lockdown in most of Europe. On the right, the average footprint

793 emission sensitivities are given at each independent station for the period of the lockdown.

794
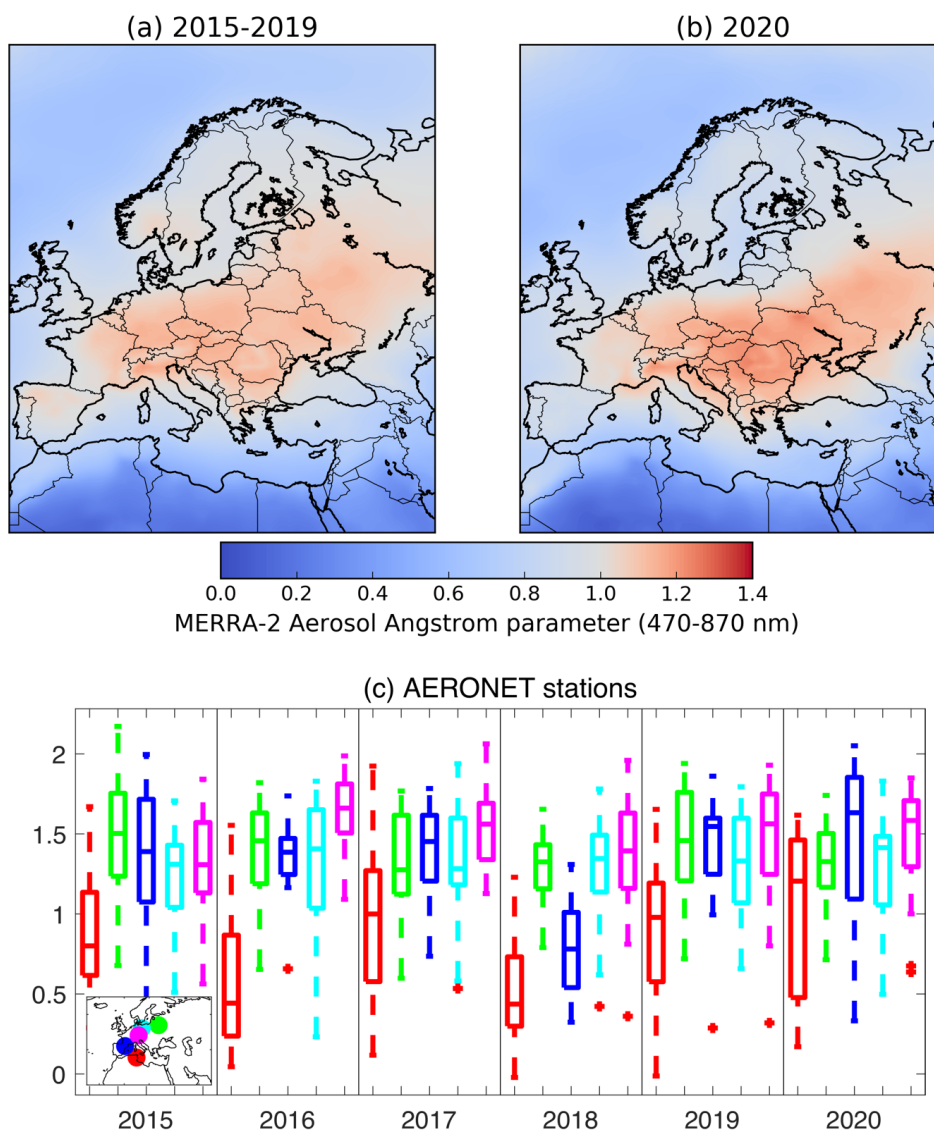
Figure 8. (a) Average total aerosol Ångström parameter (470-870 nm) over Europe (mid-
March to April) in the five previous years (2015–2019) and (b) in 2020 (lockdown). (c)
AERONET Absorption AE in Ben Salem (9.91°E, 35.55°N), Minsk (27.60°E, 53.92°N),
Montsec (0.73°E, 42.05°N), MetObs Lindenberg (14.12°E, 52.21°N) and Munich University
(11.57°E, 48.15°N) during mid-March to April in all years since 2015.
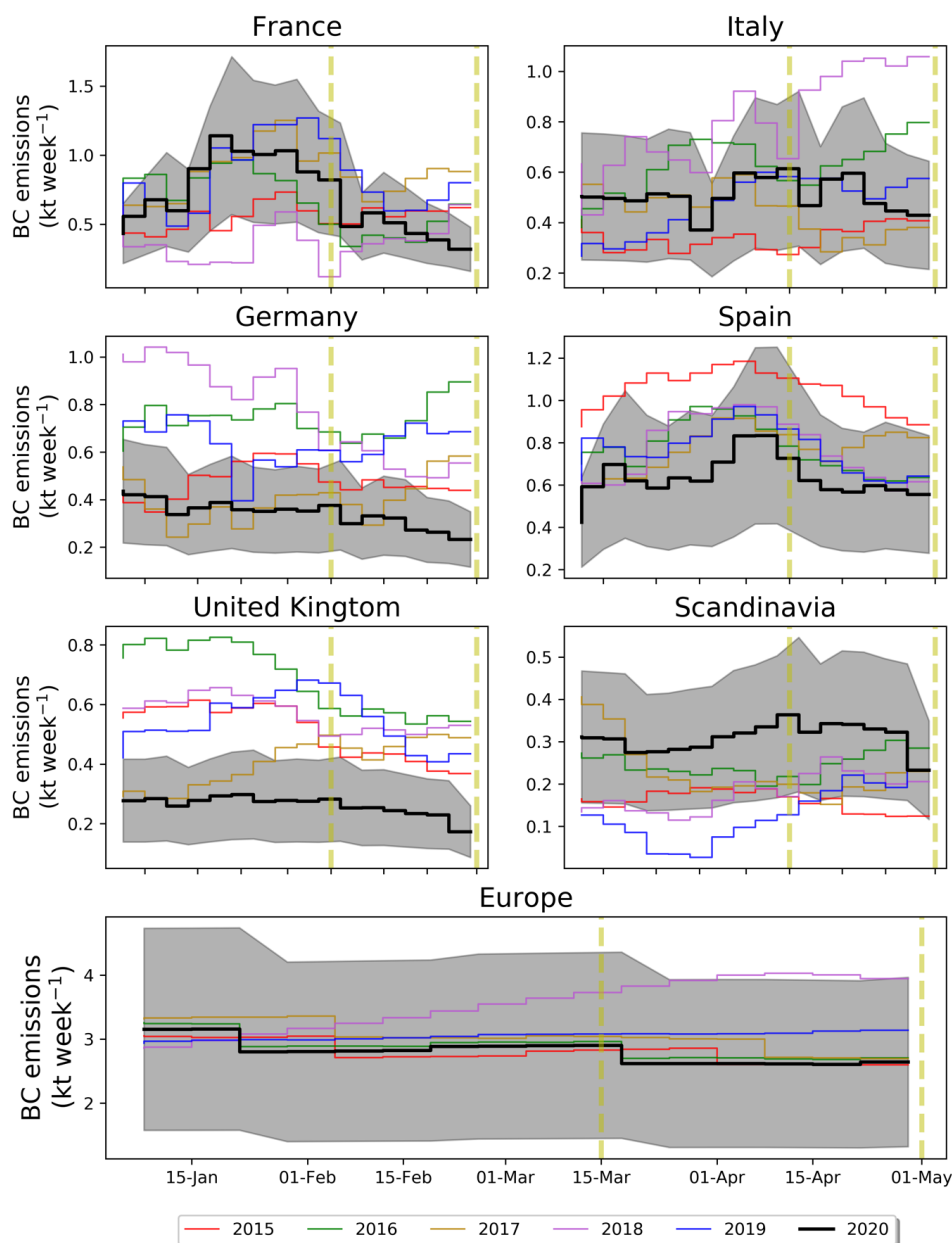
Figure 9. Posterior BC emissions in the most highly affected European countries (France, Italy, Germany, Spain and UK), Scandinavia and Europe from the COVID-19 pandemic (2020). Posterior BC emissions for every year since 2015 are also plotted in the same temporal resolution to show changes in BC emissions characteristics during the 2020 COVID-19 pandemic. The grey shaded area corresponds to the BC emission uncertainty, while the vertical yellow dashed lines correspond to the beginning and end of the 2020 lockdown.